CFD Letters

Journal homepage:
https://semarakilmu.com.my/journals/index.php/CFD_Letters/index
ISSN: 2180-1363

Influence of Blade Number on the Hydrodynamic Performance of a Propeller-Type Axial Turbine for In-Pipe Installation

Oscar Darío Monsalve-Cifuentes[1,*], Sebastián Velez-Garcia[1], Josept David Revuelta-Acosta[2]

[1] Department of Mechatronics and Electromechanics, Faculty of Engineering, Metropolitan Institute of Technology, Medellín, Colombia
[2] Department of Civil Engineering, Faculty of Engineering, Veracruzana University, Coatzacoalcos, Mexico

ARTICLE INFO

Article history:
Received 12 August 2023
Received in revised form 15 September 2023
Accepted 17 October 2023
Available online 1 January 2024

Keywords:
Number of blades; axial turbine; water turbine; in-pipe turbine; CFD; hydraulic performance

ABSTRACT

In-pipe hydraulic turbines are a promising energy-harvesting technology. Recent studies have demonstrated a strong influence of the turbine blade number on the performance of an axial propeller-type turbine. However, limited research has been dedicated to turbine diameters less than 100 mm. Therefore, this research aimed to determine the effect of the number of blades on the hydrodynamic performance of a 75.3 mm diameter axial propeller turbine for in-pipe installation. A parametric numerical study was performed by varying the angular velocity from 1600 to 3800 rpm and the number of blades from 2 to 6. Results identified an inverse correlation between the hydraulic efficiency of the turbine and its blade number and a direct correlation between the pressure head and the turbine torque. Furthermore, the performance showed hydraulic behavior comparable to those found in literature, confirming a similar hydraulic behavior as turbines with diameters exceeding 100 mm. Additionally, the turbine's internal flow behavior was analyzed by visualizing the vortex structure using the Q-criterion. Lastly, this study provides a deeper understanding of the effect of the number of blades on the hydrodynamic performance of an axial turbine for in-pipe installation.

1. Introduction

1.1 General Context and Motivation

Electric power generation, water storage [1], and distribution of water [2, 3], have become main research topics over the years because they are basic needs for society [4, 5]. Consequently, large and medium size hydraulic turbines have been used to harness energy from large rivers [6] and irrigation canals [7]. Recently, small turbines have gained popularity due to low installation costs and minimal impact on the environment. As a result, they have been adapted to mini and micro hydropower generation in small river drainage systems and sewage [8] and water distribution pipeline systems [9].

Two problems arise during the operation of water supply and distribution piping systems. The first is the overpressure generated within piping systems, which generally is controlled by pressure-

* *Corresponding author.*
E-mail address: oscarmonsalve204998@correo.itm.edu.co (Oscar Darío Monsalve Cifuentes)

https://doi.org/10.37934/cfdl.16.4.134158

regulating valves (PRV's) [10]. The second problem lies in the hydraulic energy accumulation that is not harvested. The latter is considered a source of reliable and sustainable source of energy that is environmentally friendly. As a result, technologies such as in-pipe turbines have been used to generate a pressure drop, act as pressure regulating valves, and harvest the energy surplus. In fact, in-pipe turbines are considered a promising technology that plays a significant role in the future of sustainable energy production. Thus, the harnessing of hydraulic energy via in-pipe turbines for electricity generation can be consumed locally, stored, or injected directly into the electrical interconnection network [11-13].

1.2 Literature Review

1.2.1 Type of turbines for in-pipe applications

One of the most hydraulically-efficient turbines for in-pipe installation is the propeller-type axial turbine, whose hydraulic efficiency ranges from 40 % to 76.8 %, measured experimentally using test rigs [13-17] and through computational fluid dynamics (CFD) [18-20]. The propeller-type turbine has the advantage of not requiring a pipe section modification as the Michell-Banki turbine does to match the highest efficiency values of the propeller type. Michell-Banki turbines without section pipe modifications reach efficiencies as high as 42.4 % [21, 22]. Next comes the vertical-axis Savonius turbine with variable and constant curvature blades reaching efficiencies between 28% [23, 24] and 45% [25], respectively. Then, the Darrieus type turbine is also used for this application, especially the straight-bladed Darrieus with 30% efficiency [26], the spherical with helicoidal blades with 26% [27], and the spherical Darrieus with 40% [25]. In summary, based on the literature review, we have chosen to concentrate on studying the axial propeller-type axial turbine. This turbine is distinguished for its high hydraulic efficiency values and advantageous characteristics, such as its ability to be installed without needing additional pipe section changes or modifications to enhance its hydraulic efficiency.

1.2.2 Blade number effect studies

One of the topics of paramount research interest is the effect of the blade number on the hydrodynamic performance of different types of turbines. The selection of the number of blades depends on the specific speed of the turbine [28], but some authors prefer to put the designer's freedom into practice. For example, a recent review study by Quaranta *et al.,* [29] reports that the standard number of blades for a Kaplan-type turbine of 5000 mm in diameter is 8, but there were no criteria for such selection. Similarly, Singh & Nestmann [30] studied a 200 mm diameter propeller-type turbine, for which they chose the blade number according to the chord length and blade pitch. The chosen blade number was 4, but no technical reason was provided on which the selection could rely. The authors emphasized the importance of knowing the effect of the blade number on the turbine performance. Arafin & Felayati [31] studied the effect of the blade number on the performance of a 300 mm diameter propeller for ship propulsion using CFD. They concluded that the thrust and efficiency were affected when the blade number increased. Then, to shed light on this matter, the following literature review reports studies about the influence of the blade number on the turbines' hydrodynamic performance, and the cited studies focused only on those who investigated the propeller-type axial hydraulic turbine for in-pipe installation.

In a follow-up investigation, Singh & Nestmann [32] studied theoretically and experimentally a 200 mm diameter propeller-type turbine. They aimed to develop a theoretical model that helps to elucidate the relationship between the internal hydraulic variables of the turbine and the blade

number, along with the hub-to-tip ratio. The experimental campaign tested three propellers varying from 5 to 6 blades and different hub-to-tip ratios, in which the hydraulic efficiency, among other performance parameters, was compared. The study concluded that the blade number had more influence on the performance than the hub-to-tip ratio. They also found that increasing the blade number reduced the hydraulic efficiency by 8-10%. The maximum achieved efficiency occurred for the minimum blade number studied, namely, 5 blades. The authors recommended implementing low hub-to-tip ratios and reducing blade number during the design process of a propeller-type turbine. Li & Liu [33] studied a 350 mm diameter axial turbine intending to numerically predict its performance using CFD (Computational Fluid Dynamics) and statistical analysis. Various highly efficient Kaplan-type turbine models were chosen, with blade numbers ranging from 4 to 6. The authors performed numerical calculations for each case, determining the internal flow characteristics and hydraulic losses under optimal operating conditions. The results indicated that the highest efficiencies were attained with lower blade numbers and a wider range of discharge values. However, it should be noted that the study only assessed the hydrodynamic parameters for the runner and the stationary domain individually. Further investigations are necessary to evaluate the overall system performance and confirm the persistence of the observed behavior. Byeon & Kim [34] aimed to analyze the effect of the blade number on the overall performance and internal flow characteristics of a propeller-type turbine. They performed a numerical CFD study by varying the blade number from 3 to 5. The study found that the maximum efficiency value was reached at 4 blades. But in the cases of 3 and 5 blades, the rotational speed and pressure head varied rapidly. Furthermore, the inverse relationship between the turbine efficiency and the pressure head was confirmed. Nonetheless, the authors did not report the diameter of the turbine, which is paramount for comparison purposes. Ohiemi *et al.,* [35] sought to analyze the effect of the blade number on total energy loss and turbulent dissipation by quantifying internal entropy production. The experimental and numerical study used a 219 mm diameter axial turbine with stator guide vanes. The runner blade number varied from 2 to 4. The study found that the local entropy production was caused mainly by turbulent dissipation, which increased the energy losses. Also, they evidenced that the increase in the turbine blade number positively affected the performance due to its inverse correlation with the energy losses. The highest numerical efficiency was approximately 78 % for the case of 4 blades.

A few studies have been published on propeller-type axial turbines under 100 mm in diameter. An example is the study by Kurniawan *et al.,* [36] and Nurdin *et al.,* [37], which aimed to determine the electrical power of an axial turbine varying the number of blades from 4 to 8 under different water discharge values. The experimental studies used a horizontal pipe with a turbine installed within it. The turbine was 60 mm in diameter and had a hub-to-tip ratio of 0.42. The study reported that the electrical power reached a maximum value of 23.9 W for 6 blades, then fell back progressively to 0.46 W for 8 blades. They also noticed that the axial force exerted on the turbine increased with the blade number. Another study carried out by Nishi *et al.,* [38], a methodology optimization was proposed in conjunction with an experimental and numerical study to elucidate the effect on geometrical parameters of a 68.1 mm diameter turbine, including but not limited to the blade chord length and blade angle. It was found that the hydraulic efficiency is most sensitive to geometrical parameters as the tip and mean blade angles. The performance improved by 9.1 % due to the reduction of the losses. The tip leakage vortex and vortices near the inlet hub caused the hydraulic losses. Nevertheless, the study did not address the effect of changing the blade number on the hydrodynamics of the turbine.

1.3 Objective and Main Contributions

The existing literature reveals a notable research gap concerning the influence of blade number on the performance of hydraulic axial turbines, highlighting the critical need for establishing an effective or optimized blade configuration. Furthermore, to the author's knowledge, up to two research articles have investigated the impact of the number of blades on the hydrodynamic performance of a propeller-type axial turbine with a diameter under 100 mm explicitly designed for in-pipe installation. Therefore, the primary objective of this study is to employ Computational Fluid Dynamics (CFD) numerical simulations to ascertain the relationship between variations in blade number and the hydrodynamic performance of a propeller-type axial turbine with a diameter of 75.3 mm intended for in-pipe applications. Accordingly, this study makes significant contributions by:

i. Validating the consistency of the turbine's mechanical power, torque, pressure head, and hydraulic efficiency in response to variations in blade number, aligning with previous findings conducted on turbines with diameters exceeding 100 mm.
ii. Addressing the research gap by investigating the impact of blade number on the hydrodynamic performance of propeller-type axial turbines with diameters under 100 mm, specifically for in-pipe applications.

2. Methodology

2.1 Governing Equations and Turbine Performance Parameters

The steady state Reynolds-averaged Navier-Stokes (RANS) transport equations in cartesian form for continuity and momentum are defined by Eq. (1) and Eq. (2), respectively. Note that the unsteady terms for continuity $(\partial\rho/\partial t)$ and momentum $\left(\partial\rho U_j/\partial t\right)$ are not present.

$$\frac{\partial}{\partial x_i}(\rho U_i) = 0 \tag{1}$$

$$\frac{\partial}{\partial x_j}\left(\rho U_i U_j\right) = -\frac{\partial P}{\partial x_i} + \frac{\partial}{\partial x_j}\left[\mu\left(\frac{\partial U_i}{\partial x_j}\right) - \rho\overline{u_i' u_j'}\right], \tag{2}$$

where the subindex i, j indicates the summation of cartesian components either in 2D or 3D form. $U_{i,j}$ is the mean velocity,ρ the fluid density, P is the pressure, μ is the dynamic viscosity, and u' is the fluctuating velocity component. The term $\rho\overline{u_i' u_j'}$ is known as the Reynolds stress.

The turbulence model used was the was the Menter's [39] $k-\omega$ Shear Stress Transport (SST). This model was designed to give highly accurate predictions of the amount of flow separation under adverse pressure gradients. The $k-\ \omega\ SST$ turbulence model has been used by several studies for turbomachinery simulations with satisfactory precision when comparing with experimental results [40-43].

The steady state $k-\omega$ model is composed of two transport equations, namely, the turbulent kinetic energy k, Eq. (3), and the turbulent frequency ω, Eq. (4).

$$\frac{\partial}{\partial x_j}\left(\rho U_j k\right) = \frac{\partial}{\partial x_j}\left[\left(\mu + \frac{\mu_t}{\sigma_k}\right)\frac{\partial k}{\partial x_j}\right] + P_k - \beta'\rho k\omega \tag{3}$$

$$\frac{\partial}{\partial x_j}\left(\rho U_j \omega\right) = \frac{\partial}{\partial x_j}\left[\left(\mu + \frac{\mu_t}{\sigma_\omega}\right)\frac{\partial \omega}{\partial x_j}\right] + \alpha_1\frac{\omega}{k}P_k - \beta\rho\omega^2 \tag{4}$$

where P_k is the production rate of turbulence (see CFX-Solver Theory guide [44]). However, the $k-\omega$ model alone fails to properly predict the flow separation from smooth surfaces. Therefore, a new definition for the transport of eddy-viscosity μ_t is obtained by the following limiter:

$$\mu_t = \frac{\rho \alpha_1 k}{\max(\alpha_1 \omega, S^* F_2)} \tag{5}$$

where S^* is an invariant measure of the strain rate. F_2 is one of two sets of blending functions along with F_1 defined by Eq. (6) and Eq. (7). The blending functions are critical for the success of the $k-\ \omega\ SST$ turbulence model.

$$F_1 = \tanh\left(\left[\min\left(\max\left(\frac{\sqrt{k}}{\beta'\omega y}, \frac{500\mu}{\rho\omega y^2}\right), \frac{4\rho k}{\max\left(\frac{2\rho}{\sigma_{\omega 2}\omega}\frac{\partial k}{\partial x_j}\frac{\partial \omega}{\partial x_j}, 1\times 10^{-10}\right)\sigma_{\omega 2} y^2}\right)\right]^4\right) \tag{6}$$

$$F_2 = \tanh\left(\left[\max\left(\frac{2\sqrt{k}}{\beta'\omega y}, \frac{500\mu}{\rho\omega y^2}\right)\right]^2\right) \tag{7}$$

where y represents the distance to the nearest wall. For completeness, the $k-\omega\ SST$ turbulence model constants are reported. They were determined and tuned by Menter [39] based on experimental data: $\beta' = 0.09$, $\beta = \ 0.075$, $\beta_2\ \alpha_1 = 5/9$, $\sigma_k = 2$, $\sigma_\omega = 2$, $\sigma_{\omega 2} = 1/0.856$.

Regarding the turbine performance parameters, the turbine torque is essential to determine the turbine efficiency. Thus, the turbine torque T is calculated using Eq. (8).

$$\mathrm{T} = \left(\int_s [\vec{r} \times (\bar{\bar{\tau}}\ \cdot \hat{n})] dS\right) \cdot \hat{a} \tag{8}$$

where S represents the surface of the rotating parts, $\vec{r}$ is the position vector, $\bar{\bar{\tau}}$ the total stress tensor (pressure and viscous stresses), $\hat{n}$ is a unit vector normal to the rotating surface, and $\hat{a}$ is a unit vector parallel to the axis of rotation [45].

Eq. (9) defines the pressure head ΔH, also called pressure drop, which is measured in units of length.

$$\Delta\mathrm{H} = \frac{P_2 - P_1}{\mathrm{g}\rho} \tag{9}$$

where P_1 and P_2 are the inlet and outlet total pressures measured in Pascals (Pa), g is the gravitational acceleration, and ρ is the waters' density (997 kg/m^3, as per CFX default) [46].

The hydraulic power P_H available within the pipe is defined by Eq. (10), where $Q\ (m^3/s)$ is the flow rate of the fluid flow passing through the turbine.

$$\mathrm{P_H} = \rho g \Delta H Q \tag{10}$$

The mechanical power P_{mech} produced by the turbine is defined by Eq. (11)

$$\mathrm{P_{mech}} = T\omega \tag{11}$$

where T (Nm) is the torque generated by the turbine induced by the fluid on the turbine blades, and ω (rad/s) is the angular velocity of the turbine.

The turbine efficiency η_t, defined by Eq. (12), is the power input over the output. The input and output powers are represented by the hydraulic power P_H and the mechanical power P_{mech}, respectively.

$$\eta_\mathrm{t} = \frac{P_{out}}{P_{in}} = \frac{P_{mech}}{P_H} = \frac{T\omega}{\rho \mathrm{g} \Delta \mathrm{HQ}} \tag{12}$$

2.2 Geometry of the Axial Propeller-Type Turbine

The propeller-type turbine geometry was generated according to the "blade model configuration" method developed by Ramos *et al.,* [20]. A free-vortex flow was assumed at the blade outlet for a turbine of 100 mm in diameter. The free-vortex flow satisfies the radial equilibrium theory [47], which means that the radial components of the velocity are not present, leading to a constant axial velocity through the turbine. This design method generates a circular blade profile with constant thickness of 1.7 mm. The blade geometry is a simpler blade design compared to a hydrofoil i.e., the NACA series airfoils. However, the circular blade is not symmetric due to its convex curvature. The convex curvature does not allow for a change in the flow direction. If for any reason the flow direction is reversed, the turbine orientation must be changed to properly face the incoming flow.

Furthermore, Table 1 shows the turbine bidimensional cartesian coordinates for the three design radii r_i: at the hub r_h, at the middle r_{middle}, and at the blade tip r_t. The turbine geometric parameters are the inlet and outlet blade angles β_1, β_2, respectively. The horizontal length between the leading and trailing edges L, the x-coordinates for the leading and trailing edges x_1, x_2, respectively. The circle radius r_c and its center coordinates x_c, y_c. For further detail, these geometric parameters are reported in the study of Ramos *et al.,* [20]. However, they designed a turbine for an external diameter of 100 mm, but in the present study we designed used a value of 75.3 mm for the external diameter. Lastly, the initial hydraulic design parameters were the same as those used for Ramos *et al.,* The initial hydraulic design parameters are the pressure head $H = 0.1741$ m, the flow rate $Q = 0.0034$ m^3/s, the turbine angular velocity $N = 300$ rpm, and the turbine efficiency $\eta_t = 0.98$.

Figure 1 (a) shows a frontal view of the turbine depicting the turbine tip diameter D_t, and the hub diameter D_h. According to the turbine diameters, the turbine hub-to-tip ratio $D_t/D_h = 0.5$. Figure 1 (b) presents a side view with a turbine length of 75 mm, and a bulb arc radius of 18.825 mm.

Table 1
Turbine geometric parameters

Design radius	$r_i\ (mm)$	$\beta_1\ (°)$	$\beta_2\ (°)$	$L\ (mm)$	$x_1\ (mm)$	$x_2\ (mm)$	$r_c\ (mm)$	$x_c\ (mm)$	$y_c\ (mm)$
$r_h\ (P_1)$	18.83	59.85	16.57	22.13	-11.07	11.07	38.19	21.95	19.18
$r_{middle}\ (P_3)$	28.24	48.93	20.15	33.20	-16.60	16.60	81.08	44.53	53.27
$r_t\ (P_5)$	37.65	40.72	21.40	44.26	-22.13	22.13	153.95	78.30	116.69

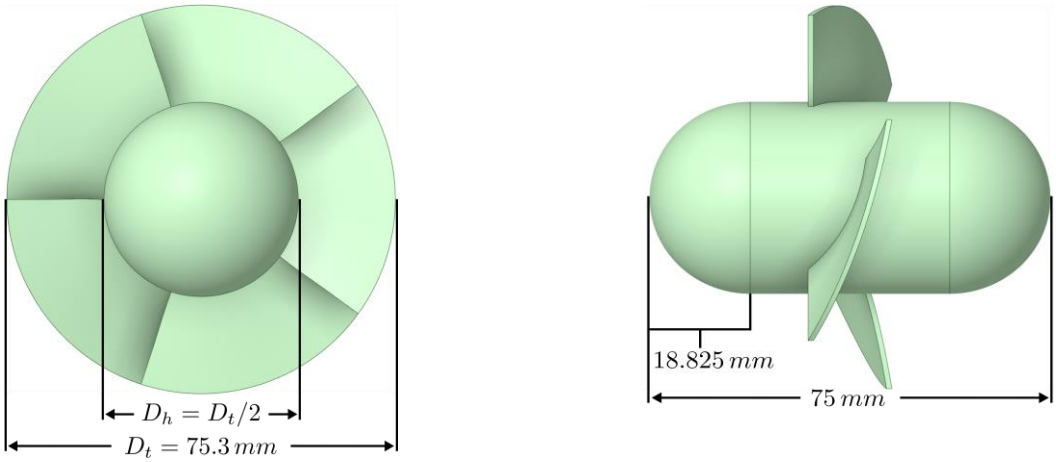

(a) (b)

Fig. 1. Propeller-type turbine three-dimensional model (a) Frontal view and characteristic diameters: D_h: hub diameter. D_t: turbine's outer diameter (b) Profile view depicting the turbine's total and bulb lengths

2.3 Computational Fluid Dynamics Simulation Setup

Section 2.3.1 discusses the boundary conditions applied to the computational fluid dynamic (CFD) simulations. Section 2.3.2 describes the grid uncertainty quantification methodology and its results. Section 2.3.3 shows the methods and parameters for generating the computational grid. Lastly, section 2.3.4 describes the parametric study carried out for the CFD simulations.

2.3.1 Boundary conditions

The CFD simulations were executed by a 12-core Intel ® Xeon CPU E5-2667 at 2.90 GHz and 32 GB of RAM workstation. We used the fluid dynamics commercial code CFX of ANSYS 2021 R2. The simulations used the Reynolds-Averaged Navier-Stokes (RANS) $k-\omega\ SST$ turbulence model [48], a frozen rotor approach, and water as the working fluid at 25 °C, assuming no heat transfer. The simulations were carried out by using a steady state analysis. This was essentially implemented because a transient simulation is out of the scope of the article. Among various applications of transient analyses is to predict the fluctuation of quantities and its effects generated by unsteady flow conditions i.e., the effect of blade tip clearance on the turbine efficiency [49], pressure fluctuations for fatigue structural analysis [50], transient hydraulic processes generated by load rejections [51], violent hydraulic instability phenomena caused by runaway conditions [52], and the startup and shutdown of hydraulic turbines [53]. However, the objective of the present study is not intended to investigate any of the exposed research topics. Furthermore, the steady state analysis is an acceptable approximation to the actual hydraulic behavior of a turbine [54, 55]. Furthermore, the steady state results can serve as the initial conditions for transient simulations, which is our intent for future works.

Figure 2 shows the control volumes and boundary conditions for the simulations. On the one hand, the control volumes were divided into a stationary domain representing the pipe with a diameter of $D_{pipe} = 77.3$ mm, and a rotational domain representing the turbine with a diameter of $D_t = 75.3$ mm. The space between the blade tip and the pipe wall is called "tip clearance t_C", which we considered for the numerical model. The tip clearance is computed as $t_C = \left(D_{pipe} - D_t\right)/2$. Given the pipe and turbine diameters, $t_c = 1$mm. The reason the tip clearance was modelled was to consider the hydraulic losses produced by tip leakage flow, which is the flow that passes through the

tip clearance. On the other hand, the stationary domain was composed of a pipe with a 90° elbow with a radius of 16.463 mm, and its length was defined in terms of the turbine diameter D_t. Therefore, the inlet-to-elbow length was specified as $4D_t$ to ensure a developed flow upstream from the turbine. The pipe length between the elbow and the turbine was defined as D_t. As the inlet portion of the pipe, the turbine-to-outlet length was defined as $4D_t$.

In Figure 2, the turbine (green color) can be distinguished between two fluid-fluid interfaces, which allows the flow to cross between the rotational and stationary control volumes. Dirichlet boundary conditions were applied to the numerical simulation as follows: an inlet boundary condition of mass flow $\dot{m} = 13.85$ kg/s with a turbulence intensity of $I = 5$ %, an outlet relative pressure boundary condition of 0 Pa (the absolute pressure was $P_{abs} = 101325\ Pa$), and the no-slip condition was applied to the pipe and turbine walls. Furthermore, the definition of the interface between the stationary and rotational domains was as a fluid-to-fluid interface because the working fluid is present at both sides at the interface location.

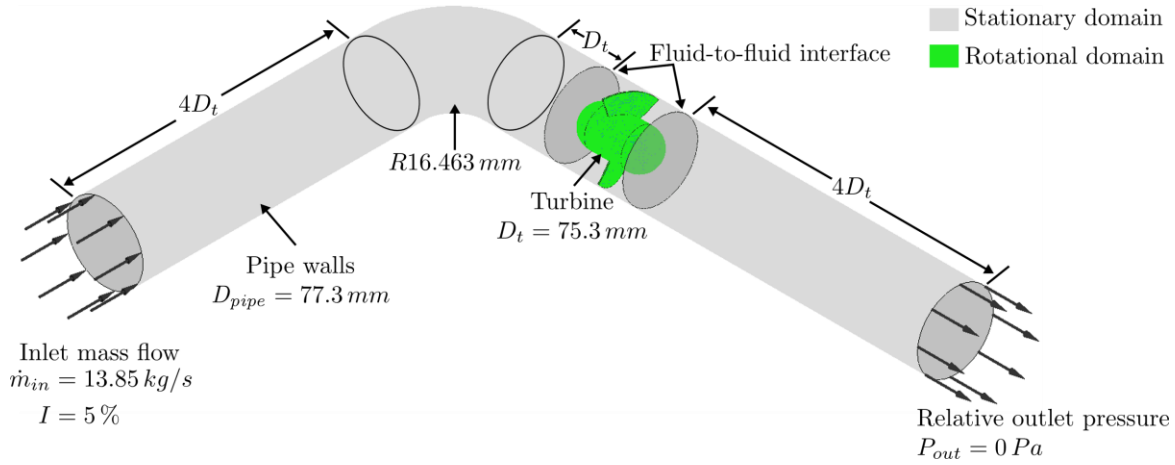

Fig. 2. Boundary conditions and control volumes for the CFD simulations

2.3.2 Grid uncertainty quantification

The Grid Convergence Index (GCI) is used to quantify the grid numerical uncertainty for the present study. The GCI method was first proposed by Roache [56], who based it on the generalized Richardson Extrapolation theory [57, 58]. The objective of the GCI method is to provide an asymptotic approach to quantify the grid uncertainty due to the finite element discretization in CFD applications. The Fluids Engineering Division of the American Society of Mechanical Engineers (ASME) adopted the application of the GCI method to encourage authors to apply it in their studies [59]. The following steps describe the GCI method application used in the present study:

i. The GCI method starts by defining a grid representative size h_i:

$$h_i = \left(\frac{1}{N_i}\right)^f \tag{13}$$

where the subscript i represents different sets of grids varying its cell count, namely, 1, 2, and 3 are the fine, medium, and coarse grids, respectively; N is the total number of cells, and for 2D $f = \frac{1}{2}$, and for 3D $f = \frac{1}{3}$. Due to the physics of the present study simulation model, $f = \frac{1}{3}$ was used.

ii. Three different grid representative sizes are computed such that $h_1 < h_2 < h_3$. Then, the grid refinement factors can be calculated as:

$$r_{21} = \frac{h_2}{h_1}, r_{32} = \frac{h_3}{h_2} \tag{14}$$

where r_{21} and r_{32} are the medium-to-fine and coarse-to-medium grid refinement factors, respectively. $r_{21}, r_{32} > 1.3$ as per ASME's recommendation [59].

iii. The solution value of interest ϕ is selected for each i_{th} grid, i.e., torque and/or pressure head. The solution values are used to calculate the differences between them as:

$$\varepsilon_{21} = \phi_2 - \phi_1, \varepsilon_{32} = \phi_3 - \phi_2 \tag{15}$$

Then, the apparent order p is calculated using Eq. (16) to Eq. (18):

$$p = \frac{|\ln|\varepsilon_{32}/\varepsilon_{21}| + q(p)|}{\ln(r_{21})} \tag{16}$$

$$q(p) = \ln\left(\frac{r_{21}^p - s}{r_{32}^p - s}\right) \tag{17}$$

$$s = 1 \times \text{sgn}(\varepsilon_{32}/\varepsilon_{21}) \tag{18}$$

On the one hand, if $r_{21} \neq r_{32}$, then a fixed-point iteration procedure must be carried out to solve for p. On the other hand, if $r_{21} = r_{32} = const.$, then $q(p) = 0$, and an iterative solution is not required. Furthermore, the convergence ratio $\varepsilon_{32}/\varepsilon_{21}$ indicates whether the GCI method can continue when a monotonic convergence is achieved $(\varepsilon_{32}/\varepsilon_{21} > 0)$, or not when an oscillatory (non-monotonic) convergence is satisfied $(\varepsilon_{32}/\varepsilon_{21} \leq 0)$ [60]. If oscillatory convergence exists, additional calculations with further grid refinements are performed. Additionally, a divergent solution is achieved if $p < 0$, and the process cannot continue. However, the absolute value on the numerator in Eq. (12) is used $(|\ln|\varepsilon_{32}/\varepsilon_{21}| + q(p)|)$ to ensure extrapolation towards $h = 0$ [61].

iv. The medium-to-fine ϕ_{ext}^{21} and coarse-to-medium ϕ_{ext}^{32} extrapolated solution values are defined by Eq. (19). These extrapolated values are the solution when the grid cells are infinitely small, i.e., $h \to 0$:

$$\phi_{ext}^{21} = \frac{r_{21}^p \phi_1 - \phi_2}{r_{21}^p - 1}, \phi_{ext}^{32} = \frac{r_{32}^p \phi_2 - \phi_3}{r_{32}^p - 1} \tag{19}$$

v. The results of the GCI method should comprise the medium-to-fine and coarse-to-medium values of the approximate relative error e_a, the extrapolated relative error e_{ext}, and the grid convergence index $\text{GCI}_{\text{fine,medium}}$. Additionally, the approximate constancy GCI should also be reported if the refinement factors are equal. Eq. (20) to Eq. (23) define these parameters:

$$e_a^{21} = \left|\frac{\phi_1 - \phi_2}{\phi_1}\right|, e_a^{32} = \left|\frac{\phi_2 - \phi_3}{\phi_2}\right| \tag{20}$$

$$e_{ext}^{21} = \left|\frac{\phi_{ext}^{21} - \phi_1}{\phi_{ext}^{21}}\right|, e_{ext}^{32} = \left|\frac{\phi_{ext}^{32} - \phi_2}{\phi_{ext}^{32}}\right| \tag{21}$$

$$GCI_{fine}^{21} = \frac{F_s e_a^{21}}{r_{21}^p - 1}, GCI_{medium}^{32} = \frac{F_s e_a^{32}}{r_{32}^p - 1} \tag{22}$$

$$GCI = \frac{GCI_{medium}^{32}}{r_{21}^p GCI_{fine}^{21}} \cong 1, only\ for\ r_{21} = r_{32} \tag{23}$$

where $F_s = 1.25$ is the security factor when the GCI method is applied to three or more different grids. However, if two grids are compared, the security factor should be $F_s = 3$ [59]. Furthermore, if the approximate constancy $GCI \cong 1$, then the solution has achieved the asymptotic range convergence and no grid refinement is needed [56, 62].

Table 2 shows the results of the GCI method applied in the present study for three different cell-count grids $N_1 =$ 13,459,846 (fine), $N_2 =$ 3,057,734 (medium), and $N_3 =$ 141,425 (coarse). The grid refinement ratios satisfy the ASME recommendation regarding its lower limit value ($r_{21}, r_{32} >$ 1.3). Since $r_{21} \neq r_{32}$, p was computed using a fix-point iteration with $p = 1$ as the initial value, see Eq. (16). For the grid solution values ϕ_i, we selected the turbine torque T, and the head drop ΔH across the turbine, defined by Eq. (8) and Eq. (9), respectively. A monotonic convergence was achieved because $\varepsilon_{32}/\varepsilon_{21}, p > 0$, which allowed the GCI method application process to continue. The apparent order p approximately matched the second order advection scheme used in CFX (High Resolution), which is a good indicator of the grid convergence. The medium-to-fine and coarse-to-medium extrapolated values ϕ_{ext}, the approximate relative error e_a, and the extrapolated relative error e_{ext} were reported. The extrapolated values ϕ_{ext}^{21}, ϕ_{ext}^{32} give an asymptotic grid solution when h tends to zero, i.e., an infinitely refined grid. It should be noted that $\phi_{ext}^{21} = \phi_{ext}^{32}$, which makes sense since there only exists one exact grid solution of T and ΔH when $h_i \to 0$. The approximate relative errors e_a^{21}, e_a^{32} consider the fine and medium grid solutions $\phi_{1,2}$ as the reference value to compute the relative error. As for the extrapolated relative errors $e_{ext}^{21}, e_{ext}^{32}$, it compares the fine and medium grid solution with respect to the extrapolated grid solution. Both the approximate and extrapolated relative errors are considered as acceptable due to the low percentage error. Furthermore, the GCI for the fine and medium grid results in low percentage values for the torque and head drop lower than 2.1 % approximately, which are within acceptable thresholds [63].

Figure 3 (a), (b) show the solution convergence for using the GCI study for the three different grid cell counts N_1, N_2 and N_3. The y-axis is represented by two grid solution values, namely, the torque T and the pressure drop ΔH. The x-axis is defined by the grid cell representative size h. A value of h close to zero signifies a more refined grid. In this manner, while h tends to zero, the grid solution values tend to a converged solution for N_3, N_2 and N_1. The value of $\phi_{ext}^{21,32}$ is the Richardson Extrapolation for the given grid solution ϕ when the grid size is infinitely refined, i.e., infinitely small grid cells. Finally, both grid solution of torque T and pressure head ΔH had a monotonically ascending trend when the grid cells became smaller, i.e., when h tends to zero.

Table 2
Result for the propeller-type turbine simulation Grid Convergence Index (GCI)

Parameters	T	ΔH
$N_1;\ N_2;\ N_3$	13,459,846; 3,057,734; 141,425	
r_{21}	1.639	1.639
r_{32}	2.786	2.786
ϕ_1	1.797 Nm	5.373 m
ϕ_2	1.778 Nm	5.327 m
ϕ_3	1.562 Nm	4.717 m
$\varepsilon_{32}/\varepsilon_{21}$	11.407	13.369
p	2.065	2.243
$\phi_{ext}^{21}, \phi_{ext}^{32}$	1.808	5.395
e_a^{21}	1.057 %	0.849 %
e_{ext}^{21}	0.592 %	0.417 %
e_a^{32}	12.18 %	11.442 %
e_{ext}^{32}	1.643 %	1.262 %
GCI_{fine}^{21}	0.745 %	0.523 %
GCI_{medium}^{32}	2.087 %	1.597 %

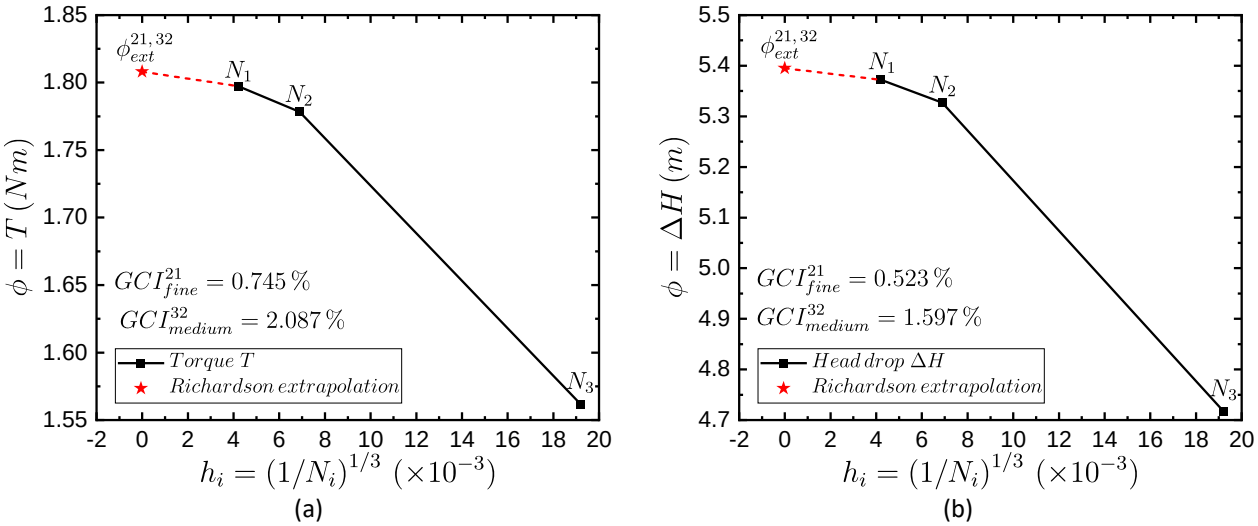

Fig. 3. Grid Converge Index (GCI) results for (a) the turbine torque and (b) pressure head

Figure 4 shows a bidimensional section visualization of the selected grid composed of a total of 3,057,734 cells. The bidimensional section is a cross sectional view of the grid to expose the rotational and stationary domain for detail purposes. The grid was obtained using the meshing module Mesh of ANSYS. The inlet and outlet of the fluid and its flow direction are depicted, alongside the stationary and rotational domains. The grid was composed of tetrahedral cells. The minimum cell sizes for the stationary and rotational domains were 5 mm and 1 mm, respectively. The details of the lower part of the rotational domain can be observed, showing the location of the fluid-fluid interfaces between rotational and stationary domains. The tip clearance $t_c = 1$ mm can be seen from the figure. The grid for the tip clearance was generated with tetrahedral cells and the same refinement parameters used for the rotational domain, which is the most refined zone of the control volume. The meshing parameters are reported in section 2.3.3. Additionally, the inflation layers applied to the blade wall are presented. According to the CFX Reference Guide [64], all ω-equation based turbulence models implement automatic wall treatment, which automatically switches from a low-Reynolds formulation

to functions based on the grid spacing provided. As recommended for the present case [65, 66], the inflation layer parameters are: first cell height of 0.01 mm, growth rate of 1.01, and 10 nodes for the number of layers.

Quality-wise, the most important grid quality parameter for a tetrahedral-type cell is the skewness. If the skewness tends to zero, the tetrahedral has the ideal shape and vice versa. The CFX theory guide [44] recommends the skewness to be less than 0.85 for any grid cell with an average value significantly lower. In this manner, the selected grid had an average skewness of 0.2174 with a maximum value of 0.807 (for 109 grid cells), a minimum of 4.25×10^{-2} (for 3.06×10^{5} grid cells), and a standard deviation of 9.794×10^{-2}. Therefore, the selected mesh is an acceptable grid quality-wise.

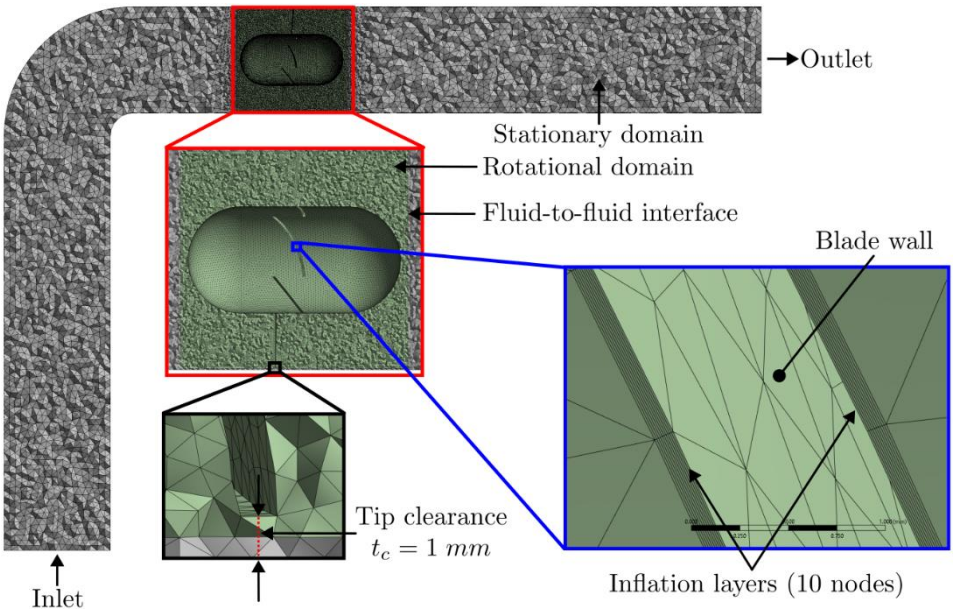

Fig. 4. Tetrahedral medium grid size N_2 with 3,057,734 cells used for the fluid dynamic simulations for the present study

2.3.3 Meshing parameters

Table 3 presents the discretization parameters used in ANSYS Mesh to generate the control volume discretization after performing the grid error quantification for the final simulations. The parameters are divided into four components: the defaults, where physics preference is selected (CFX), the element order and the global mesh size; the sizing, where detailed parameters are configured to define the mesh generation behavior; the quality, where the main target quality limit is set along the mesh smoothing; lastly, the mesh refinement methods, where localized sizing is set up. Mainly, there was no need to change most of the parameters within the sizing component due to the previous grid study results, meaning they were left to the default value. More importantly, the mesh refinement methods were defined for the rotational and stationary domain and for the interface surfaces using the sizing refinement method. For the rotational and stationary domains, and for the interfaces, the elements size was defined as 1 mm, 5 mm, 1 mm, respectively. Additionally, inflation layers were applied to the blade walls. One the one hand, the first layer thickness and the growth rate parameters were determined with previous simulation testing. On the other hand, the number of layers for the inflation method were determined as per recommendation [66].

2.3.4 Parametric study

The parametric study was performed considering two input variables: the turbine angular velocity ω, and the turbine number of blades Z. Then, for the same boundary conditions described in Figure 2, the angular velocity, ω, varied from 1600 and 3800 rpm in steps of 200 rpm and the number of blades, Z, varied from 2 to 6 blades. The output variables were the turbine torque T, and the inlet P_{in} and outlet P_{out} total pressures. Figure 5 illustrates the variation of the number of blades. Once the design of the turbine was obtained, the number of blades were changed using the circular pattern tool within the three-dimensional modeling software SpaceClaim of ANSYS.

Table 2
ANSYS Mesh discretization parameters

Component	Parameter	Detail
Defaults	Physics preference	CFD
	Solver preference	CFX
	Element order	Linear
	Element size	Default (34.087 mm)
Sizing	Use adaptative sizing	No
	Growth rate	Default (1.2)
	Max size	Default (68.173 mm)
	Mesh defeaturing	Yes
	Defeature size	Default (0.17043 mm)
	Capture curvature	Yes
	Curvature min size	Default (0.34087 mm)
	Curvature normal angle	Default (18.0 °)
	Capture proximity	Yes
	Proximity min size	Default (0.34087)
	Proximity gap factor	Default (3.0)
	Proximity size sources	Faces and edges
Quality	Check mesh quality	Yes, errors
	Target skewness	Default (0.9)
	Smoothing	High
Mesh refinement methods	Sizing at rotational domain	Element size: 1 mm
	Sizing at stationary domain	Element size: 5.0 mm
	Sizing at interfaces	Element size: 1 mm
	Inflation at blade walls	- First layer thickness: 0.01 mm. - Maximum layers: 10. - Growth rate: 1.01

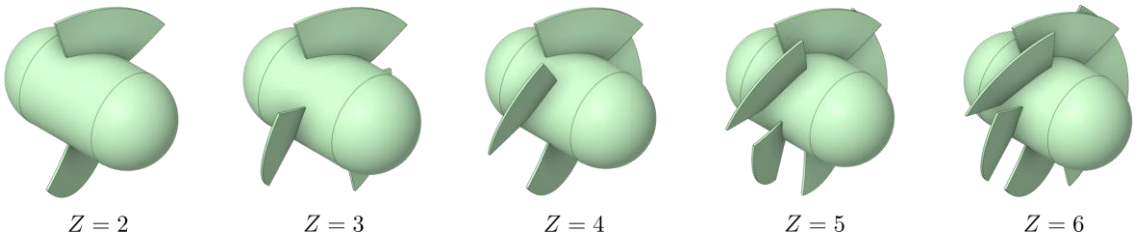

Fig. 5. Turbine blade variation from 2 to 6 for the parametric CFD study

3. Results

3.1 Turbine Performance Curves

Figure 6 presents the mechanical performance variables of the axial turbine. These variables are the torque and the mechanical power and are a function of the angular velocity ω (horizontal axis) that ranges from 1600 and 3800 rpm, and the number of blades in a range between 2 and 6. Figure 6 (a) shows a negative linear correlation between the torque and the angular velocity, namely, when the angular velocity of the turbine tends to zero, the torque tends to its maximum value. This is because the fluid exerts the maximum mechanical momentum when there is no relative rotational motion between the turbine blades and the fluid. The mentioned working point, when $\omega \to 0$ and $T \to max$ is known as stall torque [16]. The magnitude of the torque increases when there is a higher number of blades in the turbine. Otherwise, when no mechanical load is imposed on the turbine, the angular velocity tends to increase as the torque decreases, i.e., $\omega \to max$ and $T \to 0$. This working condition is referred to as runaway speed [67]. Figure 6 (b) presents the nonlinear relationship between the turbine mechanical power and the angular velocity. The mechanical power is nonlinear due to the inverse relationship between the angular velocity and torque. Additionally, it can be observed that the mechanical power increases and the number of blades increases. Lastly, the maximum point of the mechanical power of a hydraulic turbine tends to be in the middle of the angular velocity range [68].

Figure 7 shows the behavior of the hydraulic variables of the pressure head and the hydraulic efficiency of the axial turbine. These variables are also a function of the angular velocity ω (horizontal axis) in a range of ($1600 \leq \omega \leq 3800$) rpm; and the number of blades in a range of $2 \leq Z \leq 6$. Figure 7 (a) presents a negative linear relationship between pressure head and angular velocity and shows an increment of pressure head as the number of blades increases. This behavior is due to the increase in the swept area of the turbine as the number of blades increases. Figure 7 (b) reports the maximum hydraulic efficiencies are reached between 2800 and 3000 rpm. Furthermore, the lower the number of blades, the higher the efficiency. This is due to the large pressure head variations as a function of angular velocity compared to the torque variation. As reported in previous studies [32, 34], a similar mathematical trend was identified in the characteristic behavior of pressure head and hydraulic efficiency as a function of turbine angular velocity and number of blades.

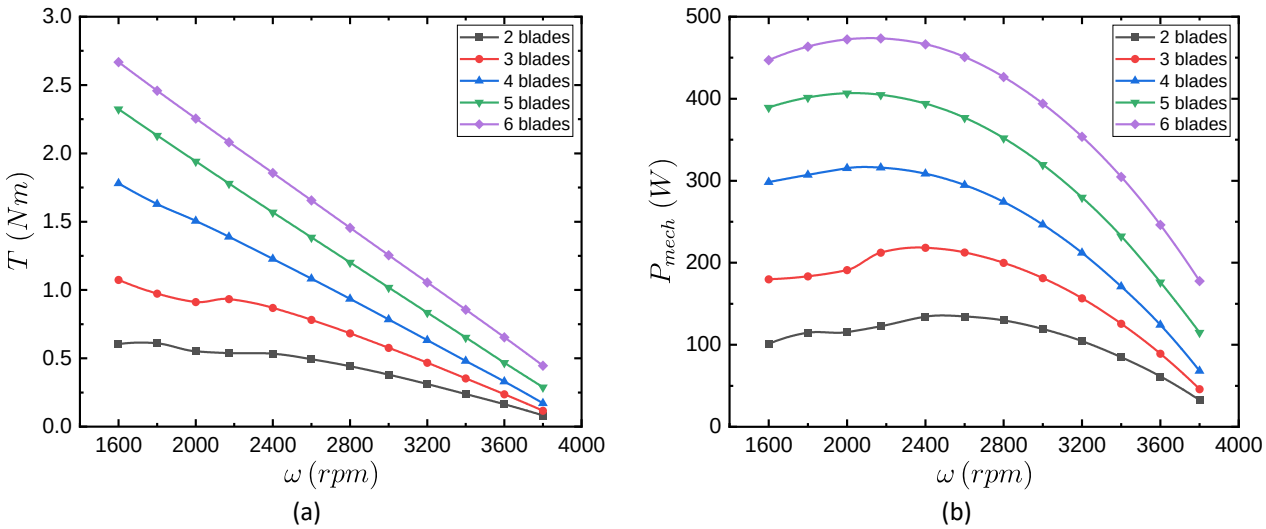

Fig. 6. Propeller-type turbine mechanical performance variables for (a) torque T and (b) mechanical power P_{mech} as a function of the angular velocity ω and the number of blades Z

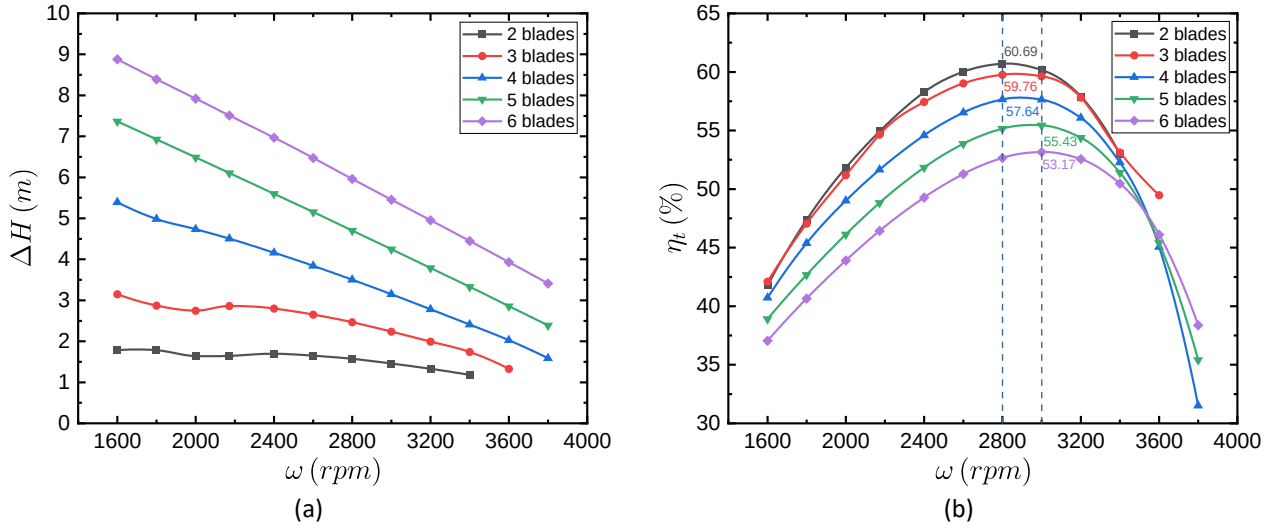

Fig. 7. Hydraulic performance variables of the axial turbine for (a) the pressure head ΔH and (b) the hydraulic efficiency η_t as a function of the angular velocity ω and the number of blades Z

3.2 Fluid Dynamic Contours

3.2.1 Total pressure and turbulence kinetic energy

Figure 8 presents the steady-state total pressure contours for the stationary domain as a function of the number of blades in the range of ($2 \leq Z \leq 6$) at a turbine angular speed of 2800 rpm. The pressure contours are defined on two bidimensional planes perpendicular to each other. According to the contour legend, blue and red colors represent the lowest and highest pressures, respectively. The figure shows the turbine in gray color, its location in the pipe domain, the fluid direction from left to right, and the zones of interest called upstream (fluid to reach the turbine) and downstream (fluid past the turbine). Based on the contours, it is possible to visually confirm that the pressure head increases with the number of blades. This is because there is a difference in pressures upstream and downstream of the turbine, which defines the pressure head ΔH. The pressure near the outlet of the pipe remains constant around a value of 4.4 kPa, while the pressure near the inlet of the fluid increases from approximately 23 kPa for two blades to 60 kPa for six blades. In the downstream region of the turbine, pressure fluctuations can be seen, mainly generated by high-velocity gradients. Moreover, the escalation in blade count induces a rise in downstream pressure relative to upstream pressure. This phenomenon stems from the fluid's heightened perception of flow blockage or constriction, consequently leading to an augmentation in upstream pressure and subsequently resulting in amplified pressures downstream.

Figure 9 presents the steady-state turbulence kinetic energy contours for the stationary domain as a function of the number of blades in the range of ($2 \leq Z \leq 6$) at a turbine angular velocity of 2800 rpm. The contours of the turbulence kinetic energy are defined on two two-dimensional planes perpendicular to each other. Regarding the contour's legend, blue and red represent the lowest and highest magnitudes, respectively. In the different contours, it is possible to visualize the turbine in gray color, its location in the pipe domain, the direction of the fluid from left to right, and the zones of interest called upstream (fluid to reach the turbine) and downstream (fluid passed the turbine). From the contours, as the number of blades increases, the turbulence kinetic energy also increases near the turbine. In other words, the turbulence kinetic energy is a measure of hydraulic losses caused by velocity and pressure gradients, wake formation that contains vortices and eddies and flow-to-turbine interaction [69], so the contour confirms the hydraulic efficiency behavior from Figure 7a.

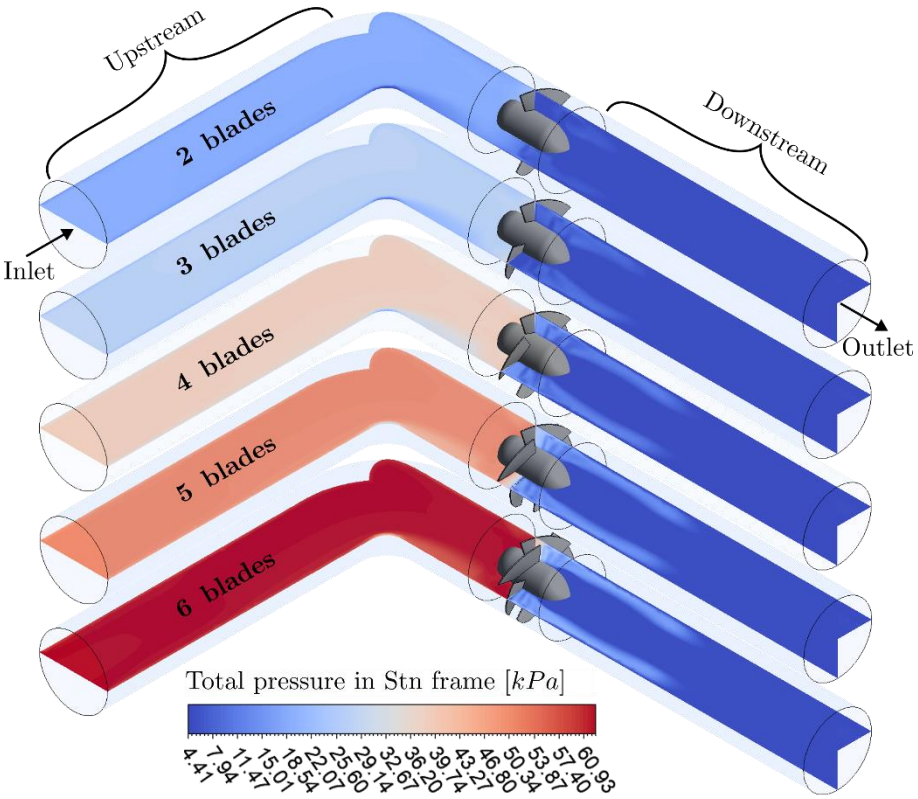

Fig. 8. Steady-state total pressure contours as a function of the number of blades Z for a turbine angular velocity of 2800 rpm

3.2.2 Vortex structures

To further visualize the effect of the number of blades on the fluid dynamics of the turbine, the vortex formation and structures are shown using the Q-criterion introduced by Hunt *et al.,* [70]. The Q.-criterion is the second invariant of the velocity gradient tensor expressed by Eq. (24).

$$\mathrm{Q} = \frac{1}{2}\left(\left|\left|\Omega^2\right|\right|_F^2 - \left|\left|S\right|\right|_F^2\right) \tag{24}$$

where Ω and S are the antisymmetric and symmetric components of the velocity gradient ∇u, i.e., $\Omega_{\mathrm{ij}} = \frac{1}{2}\left(\partial u_i/\partial x_j - \partial u_j/\partial x_i\right)$ and $S_{ij} = \frac{1}{2}\left(\partial u_i/\partial x_j + \partial u_j/\partial x_i\right)$. The operator $\left|\left|\cdot\right|\right|_F$ represents the Frobenius norm. The Q-criterion is the local balance between the vorticity magnitude Ω and the shear strain rate S. Therefore, for the Q-criterion to be able to quantify vortical flow regions, $Q > 0$ and the local pressure must be below the ambient pressure [71].

Iso-surfaces were used to render the Q-criterion to represent vortical fluid motion regions. The Q-criterion iso-surfaces were colored with the normalized helicity H_n [72], defined by Eq. (25).

$$H_n = \frac{\vec{\xi} \cdot \vec{w}}{\left|\vec{\xi}\right| \cdot \left|\vec{w}\right|} \tag{25}$$

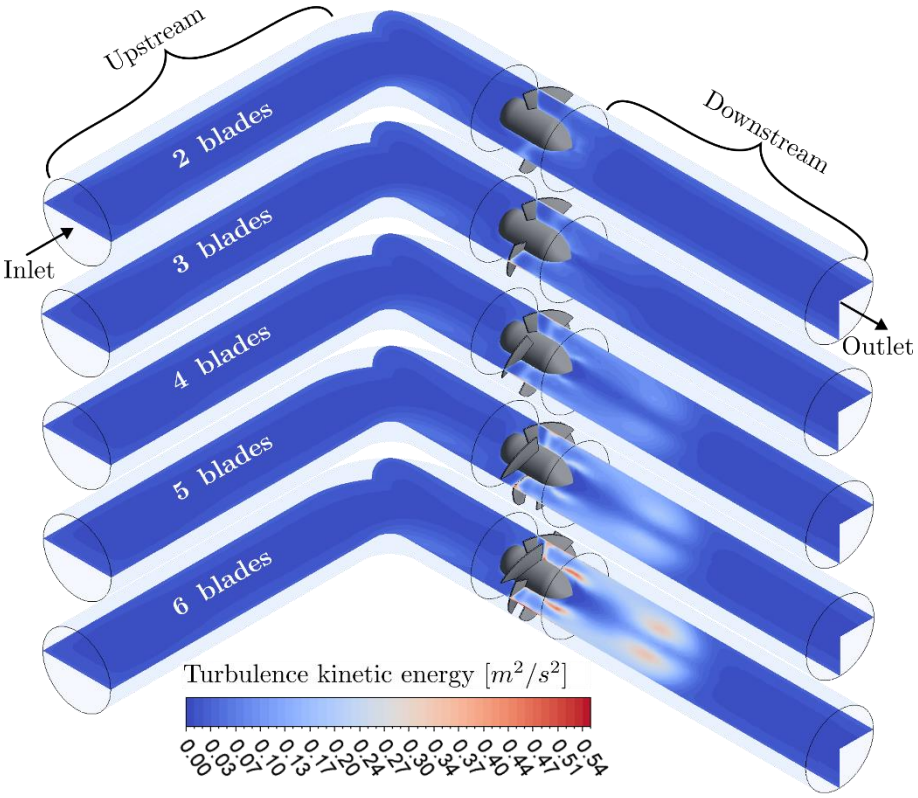

Fig. 9. Steady-state turbulence kinetic energy contours as a function of the number of blades Z for a turbine angular velocity of 2800 rpm

Where $\vec{\xi}$ is the vorticity and $\vec{w}$ is the relative velocity used to compute the helicity for the rotational domain. The relative helicity is normalized by the dot-product between the absolute value of the above vectors. The normalized helicity ranges between -1 and 1. The physical meaning of helicity elucidates valuable information about vortex structures. On the one hand, the sign of H_n indicates a vortex's swirl rotation direction relative to the stream-wise velocity direction. On the other hand, values of H_n close to the unity indicate high rotational speed and vorticity [72].

Figure 10 shows the vortex structure visualization for the turbine rotational domain for each variation of the number of blades Z from 2 to 6. The contours correspond to the best efficiency point (BEP) at a rotational speed of $\omega = 2800$ rpm. The fluid flow direction is from negative to positive X-axis, and the turbine rotates around the positive X-axis direction. Figure 10 (a) shows the vortex structures using the Q-criterion at 300000 s^{-2} colored with the dimensionless helicity H_n, where various types of vortices are identified. Each blade's interest zones are named pressure and suction surfaces (PS, SS), respectively. Although there were no vortex structures on the PS, we found the contrary for the SS and different zones downstream. At the blade's, tip leakage vortices (TLV) are formed due to the pressure differential between the PS and SS. TLV vortices stayed generally unchanged for each Z variation. The wake vortices (WV) located at the trailing edge (TE) conserved the same vortex structure but changed in H_n for the variation of Z. Additionally, the leading-edge vortices (LEV) were progressively suppressed by the increasing Z. Both the WV and TLV structures are caused by flow separation, especially because the leading and trailing edges of the blades were blunt. At the turbine hub, structures called horseshoe vortices (HV) were formed due to the interaction between the LE and TE at the blade passage. HV followed spiral trajectories and they increased their size in direct proportion to Z and inversely with the blade passage size. Also, at the end of the downstream bulb, longitudinal vortices (LV) started to form as follows: when $Z = 2$, there were spiral vortex structure formations, but for $Z \geq 3$, the spiral vortices transitioned to LV's; for the

case of $Z = 3, 4$, LV's had opposite rotational direction (blue and red color), but for $Z = 5, 6$ all the LV's had the same rotational direction (all in red color); lastly, as Z increased, the HV structures covered progressively the hub area, until they merged completely with the LV structures at $Z = 6$.

Figure 10 (b) shows the Q-criterion contour ranges from 0 to 180000 s^{-2}. These contours were placed on $Y - Z$ planes located at $X = 0.01$ m (first plane) and $X = 0.037$ m (second plane) relative to the turbine center. On the first plane, the contours help to elucidate the vortex cores (VC) of the TLV structures. We confirmed that the number of vortex cores matched the number of blades Z and that the maximum values of the Q-criterion correspond to the location of the vortex cores. The tip leakage vortices of a propeller-type turbine usually form downstream along a spiral trajectory, and the spiral vortices form at the end of the downstream bulb. On the one hand, the main spiral vortex structure at the hub seen in the second plane for $Z = 2$ transitioned to LV ring-like structures at the center of the contours for $Z \geq 3$. On the other hand, the TLV's located at the vortex cores dissipated quickly from a main spiral vortex structure to secondary spiral vortex formations seen on the second plane for the cases $Z = 3, 4, 5$.

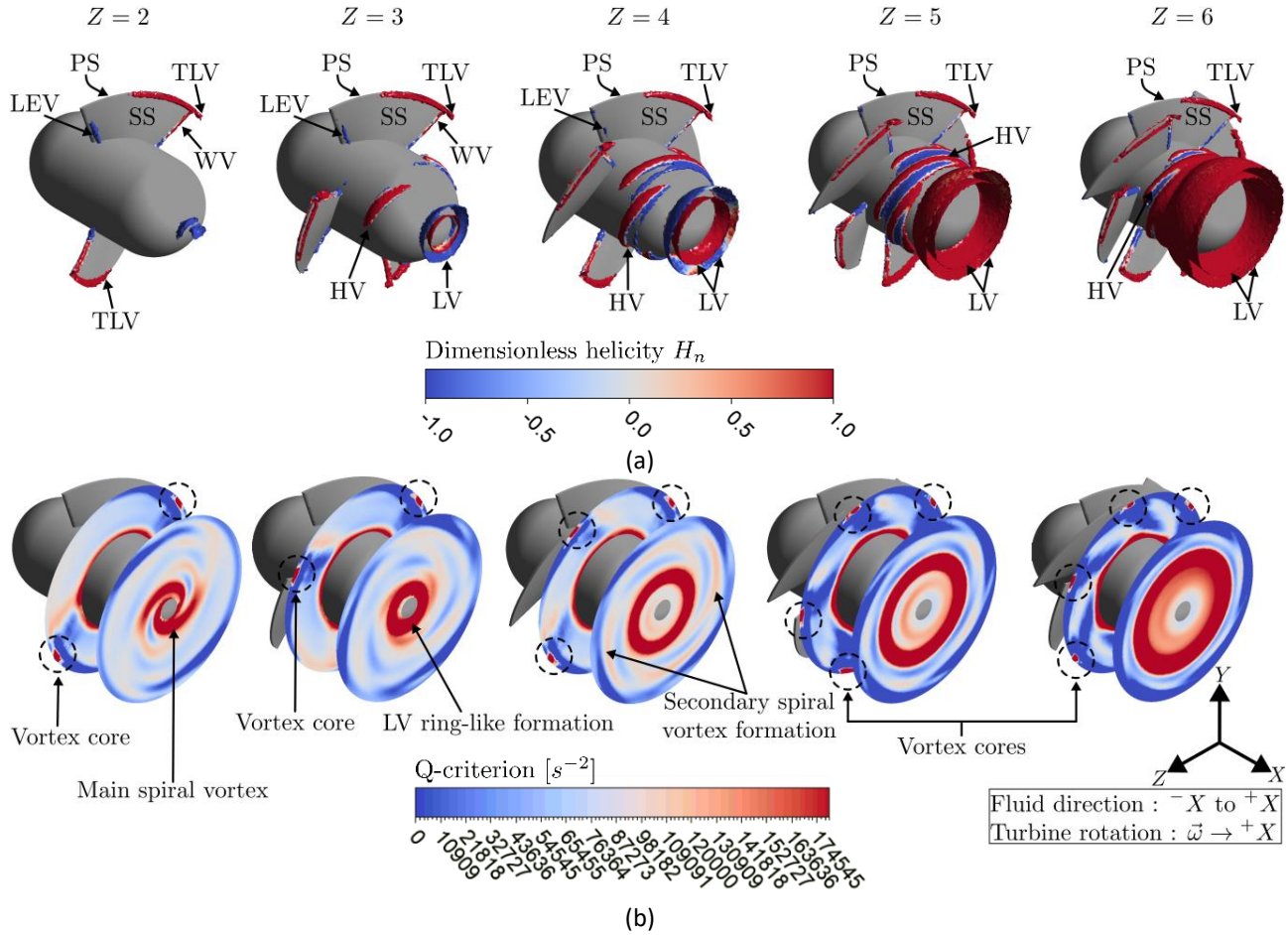

Fig. 10. (a) Rotational domain iso-surface vortex visualization for $N = 2800$ rpm through the Q-criterion at 300000 s^{-2} colored with the dimensionless helicity H_n. (b) Rotational domain Y-Z plane contours placed relative to the turbine's center at $X = 0.01\ m$ and $X = 0.037\ m$ colored with the Q-criterion in range of 0 to 180000 s^{-2}

Figure 11 shows the stationary domain iso-surfaces vortex visualization using the Q-criterion at 20000 s^{-2} colored with the dimensionless helicity H_n. The contours correspond to the BEP at a rotational speed of $\omega = 2800$ rpm. For the case $Z = 2$, the main spiral vortex formation of two structures can be seen as well as some tip leakage vortex (TLV) formations. These last vortices appear

to be within the rotational domain, but in fact they are located within the stationary domain, specifically in the clearance space between the blade tips and the pipe wall (not shown). For $Z = 3$, the longitudinal vortex (LV) formation near the bulb is visible, but it quickly dissipates to secondary spiral vortices. For the cases of $Z = 4, 5, 6$, we identified the LV main structure formation and its rotational direction uniformization. The shape of the LV's can be compared to the contours shown in Figure 10 (b), in which they grow in diameter and tend to rotate in the same direction as Z increases. The vortex structures for each variation of $Z = 2, 3, 4, 5, 6$ completely dissipated at an approximately location of $X =$ (0.077, 0.105, 0.157, 0.165, 0.173) m, respectively. The constant increasing size of the vortex LV structures with the increasing Z is directly related to the hydraulic loses, which can be confirmed by contours of the turbulence kinetic energy seen in Figure 9.

Vortex structures arise due to the complex interaction between the turbine blades, the fluid flow, and the confined geometry of the pipe. The presence of these structures can lead to both advantageous and challenging consequences. From a practical standpoint, the appearance of longitudinal vortex structures can impact the turbine's efficiency and performance. The rotational motion of these vortices can induce additional turbulence in the downstream flow, altering the velocity profiles and pressure distribution. This altered flow environment may lead to increased energy losses, reduced turbine efficiency, and changes in the turbine's operational stability [73]. The physical implications extend beyond performance metrics. Longitudinal vortex structures can affect the mechanical integrity of the turbine. Cyclic loading from vortex shedding and unsteady flow can subject the turbine blades and components to fluctuating forces, potentially leading to fatigue, wear, and even structural damage over time [74].

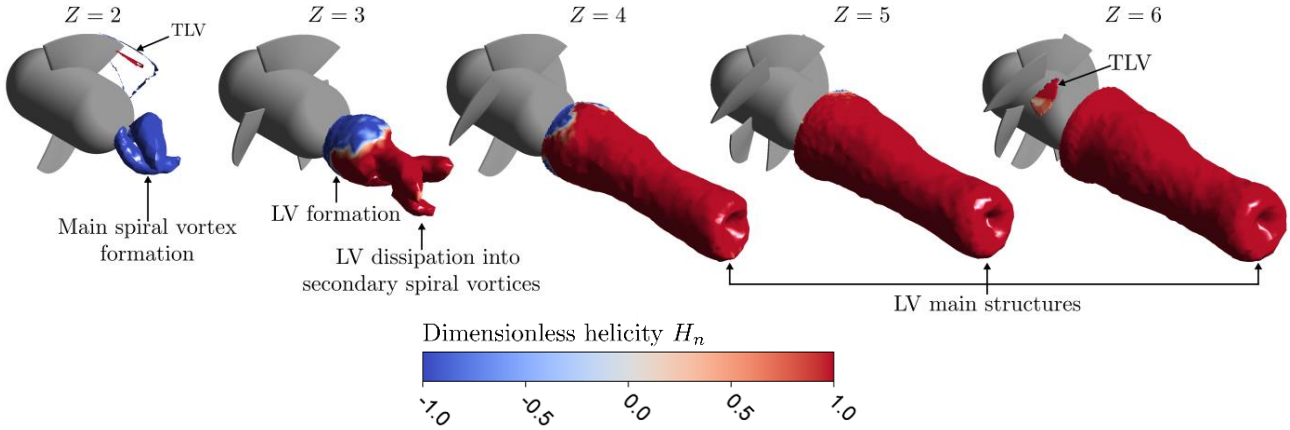

Fig. 11. Stationary domain iso-surface vortex visualization using the Q-criterion at 20000 s^{-2} colored with the dimensionless helicity H_n for $N = 2800$ rpm

Figure 12 provides insight into the formation of vortices within the stationary domain of a turbine as a function of blade count and turbine rotational speed. The choice to depict these vortices in the stationary domain is motivated by their role in generating downstream longitudinal vortex structures, which directly impact the turbine's performance by causing adverse hydraulic and mechanical effects. Notably, the figure illustrates that an increase in blade count leads to larger diameters of longitudinal vortices (LV's), resulting in an augmentation of the mechanical power extracted from the fluid by the turbine. This effect is attributed to the increased blade count, which reduces the available area for fluid passage, thereby creating steeper fluid velocity gradients conducive to the formation of longitudinal vortices. Additionally, these velocity gradients result in higher pressure differentials on the blade surfaces, thus enhancing the turbine's mechanical power. This deduction stems from a combined analysis of Figure 6 (b) and Figure 12. Furthermore, it is evident that the presence of spiral and longitudinal vortex structures decreases as blade count

increases and turbine angular velocity rises. This phenomenon arises due to higher angular velocities tending to equalize upstream and downstream pressures of the turbine, leading to reduced pressure differentials (see Figure 7 (a)). In contrast, a greater pressure delta increases the likelihood of vortex generation. These observations facilitate an understanding of vortex behavior concerning angular velocity. Figure 12 also reveals that as blade count and turbine angular velocity increase, the predominance of spiral vortices diminishes, making way for longitudinal vortices. However, continued growth in blade count and turbine angular velocity causes vortices to disperse, as previously elucidated in this paragraph. Finally, summarizing our findings, the maximum hydraulic efficiency achieved was 60.69% at an angular velocity of 2800 rpm, a pressure head of 1.57 m, mechanical power of 129.63 W, and a torque of 0.44 Nm. Notably, we observed that changes in pressure head were more sensitive to shifts in angular velocity than to variations in torque. This trend led us to discover that optimal turbine efficiencies were associated with a lower number of blades. This behavior can be attributed to the increased formation of vortex structures as the number of blades rises, resulting in higher turbulence kinetic energy and associated hydraulic losses. These findings carry implications for the deployment of in-pipe turbines. For applications seeking higher pressure drop and maximum mechanical power output, using more blades is a suitable choice. However, for efficient operation with reduced pressure drop, fewer blades are recommended. Interestingly, our study agrees with prior research by highlighting that, in general, higher hydraulic efficiencies are linked to a lower blade count. These insights enhance our understanding of in-pipe turbine dynamics and provide practical guidance for optimizing their performance across various scenarios.

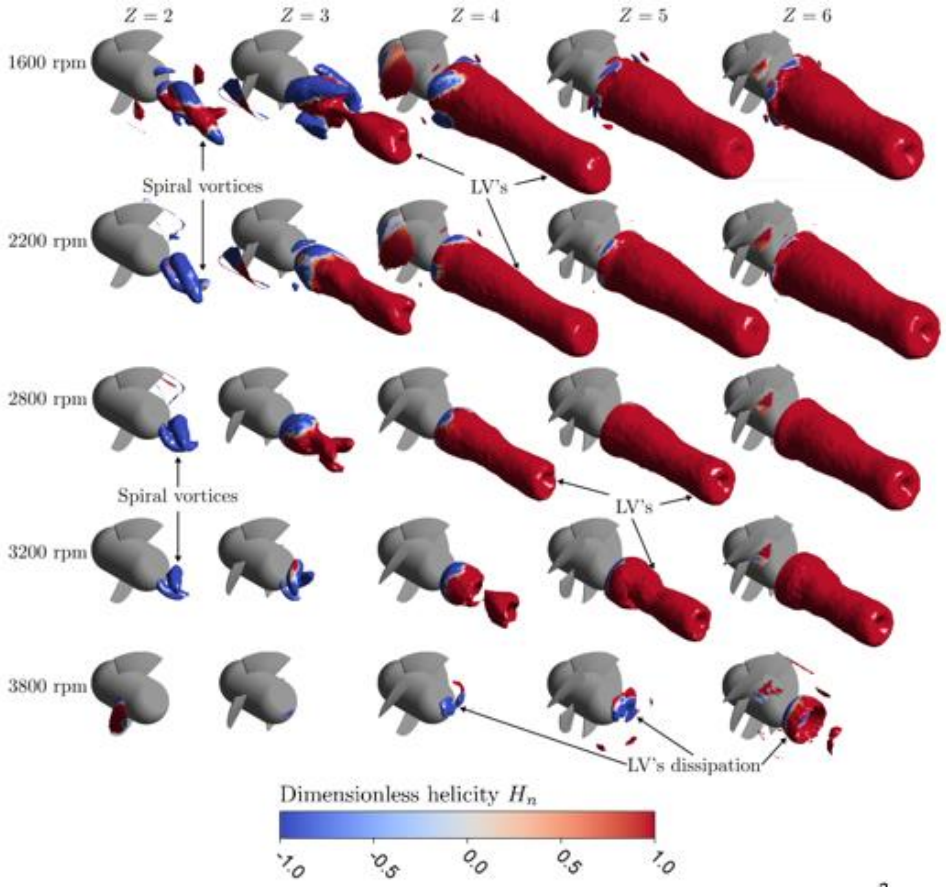

Fig. 12. Stationary domain iso-surface vortex visualization using the Q-criterion at 20000 s^{-2} colored with the dimensionless helicity H_n as function of the blade number Z and the turbine angular velocity

4. Conclusions

A numerical simulation of a 75.3 mm diameter propeller-type axial turbine was conducted within a 77.3 mm diameter pipe to investigate its performance. A parametric computational fluid dynamics (CFD) study was performed, varying the angular velocity from 1600 to 3800 rpm and the number of blades from 2 to 6. The results reveal several key findings. Firstly, the torque and pressure head exhibit an inverse relationship with angular velocity but a direct relationship with the number of blades. Conversely, the hydraulic efficiency demonstrates an inverse correlation with the turbine's blade number.

The highest hydraulic efficiency achieved was 60.69 % at an angular velocity of 2800 rpm, a pressure head of 1.57 m, a mechanical power of 129.63 W, and a torque of 0.44 Nm. The study observed that the pressure head varies more significantly with angular velocity compared to torque, resulting in the highest turbine efficiencies being attained with a lower number of blades. This hydraulic behavior can be attributed to the intensified formation of vortex structures as the blade number increases, consequently leading to elevated turbulence kinetic energy and associated hydraulic losses. This means the fewer vortex structures, the better for the overall turbine performance.

If the objective of utilizing turbines for in-pipe applications is to generate a higher pressure drop while maximizing mechanical power output, employing a higher number of blades is a suitable option. However, for efficient operation with reduced pressure drop, employing fewer blades is recommended. In contrast to previous studies, our findings indicate that, for the most part, a lower number of blades results in higher hydraulic efficiencies.

For future investigations, it is essential to further explore the effect of blade number on hydraulic performance for turbines equipped with stator guide vanes, as our results differ from those reported by Ohiemi *et al.,* [35].

Acknowledgement

This research was not funded by any grant. However, the authors thank the support of the investigation line of Advanced Computing and Digital Design −CADD− from the Instituto Tecnológico Metropolitano from Medellín, Colombia, for providing the workstation for the numerical simulations.

References

[1] Slavik, Irene, Keila Roberta Oliveira, Peter Batista Cheung, and Wolfgang Uhl. "Water quality aspects related to domestic drinking water storage tanks and consideration in current standards and guidelines throughout the world–a review." *Journal of water and health* 18, no. 4 (2020): 439-463. https://doi.org/10.2166/wh.2020.052.

[2] Bonilla-Granados, C. A., N. J. Cely-Calixto, and GA Carrillo Soto. "Hydraulic optimization of the physical parameters of a drinking water distribution system." In *Journal of Physics: Conference Series*, vol. 2139, no. 1, p. 012013. IOP Publishing, 2021. https://doi.org/10.1088/1742-6596/2139/1/012013.

[3] Weston, S. L., R. P. Collins, and J. B. Boxall. "An experimental study of how hydraulic transients cause mobilisation of material within drinking water distribution systems." *Water Research* 194 (2021): 116890.. https://doi.org/10.1016/j.watres.2021.116890.

[4] Barton, Neal Andrew, Timothy Stephen Farewell, Stephen Henry Hallett, and Timothy Francis Acland. "Improving pipe failure predictions: Factors affecting pipe failure in drinking water networks." *Water research* 164 (2019): 114926. https://doi.org/10.1016/j.watres.2019.114926.

[5] Kohlitz, Jeremy, Joanne Chong, and Juliet Willetts. "Rural drinking water safety under climate change: the importance of addressing physical, social, and environmental dimensions." *Resources* 9, no. 6 (2020): 77. https://doi.org/10.3390/resources9060077.

[6] Kirke, Brian. "Hydrokinetic turbines for moderate sized rivers." *Energy for Sustainable Development* 58 (2020): 182-195. https://doi.org/10.1016/j.esd.2020.08.003.

[7] Shashikumar, C. M., Hindasageri Vijaykumar, and Madav Vasudeva. "Numerical investigation of conventional and tapered Savonius hydrokinetic turbines for low-velocity hydropower application in an irrigation channel." *Sustainable Energy Technologies and Assessments* 43 (2021): 100871. https://doi.org/10.1016/j.seta.2020.100871.

[8] Nishi, Yasuyuki, Ryouta Suzuo, Daichi Sukemori, and Terumi Inagaki. "Loss analysis of gravitation vortex type water turbine and influence of flow rate on the turbine's performance." *Renewable Energy* 155 (2020): 1103-1117. https://doi.org/10.1016/j.renene.2020.03.186.

[9] (!!! INVALID CITATION !!! [9-11]).

[10] Pasha, M. Fayzul K., Matthew Weathers, and Brennan Smith. "Investigating energy flow in water-energy storage for hydropower generation in water distribution systems." *Water Resources Management* 34 (2020): 1609-1622. https://doi.org/10.1007/s11269-020-02497-5.

[11] Ramos, H. M., M. Mello, and P. K. De. "Clean power in water supply systems as a sustainable solution: from planning to practical implementation." *Water science and technology: water supply* 10, no. 1 (2010): 39-49. https://doi.org/10.2166/ws.2010.720.

[12] Sammartano, Vincenzo, Costanza Aricò, Armando Carravetta, Oreste Fecarotta, and Tullio Tucciarelli. "Banki-Michell optimal design by computational fluid dynamics testing and hydrodynamic analysis." *Energies* 6, no. 5 (2013): 2362-2385. https://doi.org/10.3390/en6052362.

[13] Saoutieff, Elise, Pierre Gasnier, Sébastien Boisseau, Javier Ojer-Aranguren, and Isabelle Rodot. "Performances of a cm-scale water flow energy harvester in real environment for autonomous flowmeters." In *Journal of Physics: Conference Series*, vol. 1407, no. 1, p. 012074. IOP Publishing, 2019. https://doi.org/10.1088/1742-6596/1407/1/012074.

[14] Nan, Ding, Toru Shigemitsu, Shengdun Zhao, Tomofumi Ikebuchi, and Yasutoshi Takeshima. "Study on performance of contra-rotating small hydro-turbine with thinner blade and longer front hub." *Renewable Energy* 117 (2018): 184-192. https://doi.org/10.1016/j.renene.2017.10.046.

[15] Nishi, Yasuyuki, Tomoyuki Kobori, Nozomi Mori, Terumi Inagaki, and Norio Kikuchi. "Study of the internal flow structure of an ultra-small axial flow hydraulic turbine." *Renewable energy* 139 (2019): 1000-1011. https://doi.org/10.1016/j.renene.2019.03.004.

[16] Samora, Irene, Vlad Hasmatuchi, Cécile Münch-Alligné, Mário J. Franca, Anton J. Schleiss, and Helena M. Ramos. "Experimental characterization of a five blade tubular propeller turbine for pipe inline installation." *Renewable Energy* 95 (2016): 356-366. https://doi.org/10.1016/j.renene.2016.04.023.

[17] Ryosuke, Sonohata, Fukutomi Junichiro, and Toru Shigemitsu Toru. "Study on contra-rotating small-sized axial flow hydro turbine." *Open Journal of Fluid Dynamics* 2012 (2012). https://doi.org/10.4236/ojfd.2012.24A039.

[18] Cifuentes, Oscar Darío Monsalve, Jonathan Graciano Uribe, and Diego Andrés Hincapié Zuluaga. "Numerical Simulation of a Propeller-Type Turbine for In-Pipe Installation." *Journal of Advanced Research in Fluid Mechanics and Thermal Sciences* 83, no. 1 (2021): 1-16. https://doi.org/10.37934/arfmts.83.1.116.

[19] Nishi, Yasuyuki, Yutaka Kobayashi, Terumi Inagaki, and Norio Kikuchi. "The design method of axial flow runners focusing on axial flow velocity uniformization and its application to an ultra-small axial flow hydraulic turbine." *International Journal of Rotating Machinery* 2016 (2016). https://doi.org/10.1155/2016/5390360.

[20] Ramos, Helena M., Mariana Simão, and A. Borga. "Experiments and CFD analyses for a new reaction microhydro propeller with five blades." *Journal of Energy Engineering* 139, no. 2 (2013): 109-117. https://doi.org/10.1061/(ASCE)EY.1943-7897.0000096.

[21] Sammartano, Vincenzo, Marco Sinagra, Pasquale Filianoti, and Tullio Tucciarelli. "A Banki–Michell turbine for in-line water supply systems." *Journal of Hydraulic Research* 55, no. 5 (2017): 686-694. https://doi.org/10.1080/00221686.2017.1335246.

[22] Sinagra, Marco, Calogero Picone, Costanza Aricò, Antonio Pantano, Tullio Tucciarelli, Marwa Hannachi, and Zied Driss. "Impeller Optimization in crossflow hydraulic turbines." *Water* 13, no. 3 (2021): 313. https://doi.org/10.3390/w13030313.

[23] Payambarpour, S. Abdolkarim, and Amir F. Najafi. "Experimental and numerical investigations on a new developed Savonius turbine for in-pipe hydro application." *Proceedings of the Institution of Mechanical Engineers, Part A: Journal of Power and Energy* 234, no. 2 (2020): 195-210. https://doi.org/10.1177/0957650919854583.

[24] Payambarpour, S. Abdolkarim, Amir F. Najafi, and Franco Magagnato. "Investigation of blade number effect on hydraulic performance of in-pipe hydro savonius turbine." *International Journal of Rotating Machinery* 2019 (2019). https://doi.org/10.1155/2019/8394191.

[25] Yang, Wei, Yimin Hou, Huiting Jia, Benqing Liu, and Ruofu Xiao. "Lift-type and drag-type hydro turbine with vertical axis for power generation from water pipelines." *Energy* 188 (2019): 116070. https://doi.org/10.1016/j.energy.2019.116070.

[26] Y. Mutlu and M. Çakan. "Evaluation of in-pipe turbine performance for turbo solenoid valve system." *Engineering Applications of Computational Fluid Mechanics* 12, no. 1 (2018): 625-634. https://doi.org/10.1080/19942060.2018.1506364.

[27] Langroudi, A. Tahadjodi, F. Zare Afifi, A. Heyrani Nobari, and A. F. Najafi. "Modeling and numerical investigation on multi-objective design improvement of a novel cross-flow lift-based turbine for in-pipe hydro energy harvesting applications." *Energy conversion and management* 203 (2020): 112233. https://doi.org/10.1016/j.enconman.2019.112233.

[28] Höfler, E., B. Širok, and A. Bergant. "Mixed-flow vertical tubular hydraulic turbine: determination of proper design duty point." *Forschung im Ingenieurwesen* 75, no. 4 (2011): 197-208. https://doi.org/10.1007/s10010-011-0145-4.

[29] Quaranta, Emanuele, Amir Bahreini, Alireza Riasi, and Roberto Revelli. "The Very Low Head Turbine for hydropower generation in existing hydraulic infrastructures: State of the art and future challenges." *Sustainable Energy Technologies and Assessments* 51 (2022): 101924. https://doi.org/10.1016/j.seta.2021.101924.

[30] Singh, Punit, and Franz Nestmann. "Experimental optimization of a free vortex propeller runner for micro hydro application." *Experimental Thermal and Fluid Science* 33, no. 6 (2009): 991-1002. https://doi.org/10.1016/j.expthermflusci.2009.04.007.

[31] Arifin, Mohammad Danil, and Frengki Mohamad Felayati. "Numerical Study of Kaplan Series Propeller using CFD: Effect of Angle of Attack and Number of Blade Variations." *CFD Letters* 15, no. 8 (2023): 200-213. https://doi.org/10.37934/cfdl.15.8.200213.

[32] Singh, Punit, and Franz Nestmann. "Experimental investigation of the influence of blade height and blade number on the performance of low head axial flow turbines." *Renewable Energy* 36, no. 1 (2011): 272-281. https://doi.org/10.1016/j.renene.2010.06.033.

[33] Li, Yunzhe, and Qilin Liu. "Analysis of hydraulic performance for Kaplan turbine components based on CFD simulation." In *IOP Conference Series: Earth and Environmental Science*, vol. 510, no. 2, p. 022038. IOP Publishing, 2020. https://doi.org/10.1088/1755-1315/510/2/022038.

[34] Byeon, Sun-Seok, and Youn-Jea Kim. "Influence of blade number on the flow characteristics in the vertical axis propeller hydro turbine." *International Journal of Fluid Machinery and Systems* 6, no. 3 (2013): 144-151. https://doi.org/10.5293/IJFMS.2013.6.3.144.

[35] Ohiemi, Israel Enema, Yang Sunsheng, Punit Singh, Yanjun Li, and Fareed Osman. "Evaluation of energy loss in a low-head axial flow turbine under different blade numbers using entropy production method." *Energy* 274 (2023): 127262. https://doi.org/10.1016/j.energy.2023.127262.

[36] Kurniawan, R., D. A. Himawanto, and P. J. Widodo. "The performance of numbers of blade towards picohydro propeller turbine." In *IOP Conference Series: Materials Science and Engineering*, vol. 508, no. 1, p. 012057. IOP Publishing, 2019. https://doi.org/10.1088/1757-899x/508/1/012057.

[37] Nurdin, Akhmad, Dwi Aries Himawanto, and Syamsul Hadi. "THE UTILIZATION OF HORIZONTAL PIPELINE FOR A STATIC BULB TURBINE AND THE DETERMINATION OF OPTIMUM BLADE NUMBER USING FLOW SIMULATION."

[38] Nishi, Yasuyuki, Nozomi Mori, Naoki Yamada, and Terumi Inagaki. "Study on the design method for axial flow runner that combines design of experiments, response surface method, and optimization method to one-dimensional design method." *Renewable Energy* 185 (2022): 96-110. https://doi.org/10.1016/j.renene.2021.12.009.

[39] Menter, Florian R. "Two-equation eddy-viscosity turbulence models for engineering applications." *AIAA journal* 32, no. 8 (1994): 1598-1605. https://doi.org/10.2514/3.12149.

[40] Amjadi, Hosain, Morteza Khashehchi, and Jaber Soltani. "Experimental investigation and numerical simulation of an inline low-head microhydroturbine for applications in water pipelines." *IET Renewable Power Generation* 14, no. 16 (2020): 3209-3219. https://doi.org/10.1049/iet-rpg.2019.1283.

[41] Junginger, Bernd, and Stefan Riedelbauch. "Numerical Investigation of a Full Load Operation Point for a Low Head Propeller Turbine." In *High Performance Computing in Science and Engineering'15: Transactions of the High Performance Computing Center, Stuttgart (HLRS) 2015*, pp. 435-447. Springer International Publishing, 2016. https://doi.org/10.1007/978-3-319-24633-8_28.

[42] Junginger, Bernd, and Stefan Riedelbauch. "Numerical Analysis of a Propeller Turbine Operated in Part Load Conditions." In *High Performance Computing in Science and Engineering'17: Transactions of the High Performance Computing Center, Stuttgart (HLRS) 2017*, pp. 355-368. Springer International Publishing, 2018. https://doi.org/10.1007/978-3-319-68394-2_21.

[43] Ocepek, Matic, Zlatko Peršin, Igor Kern, Vesko Djelić, Simon Muhič, and Andrej Lipej. "Experimental and numerical analysis of cavitation and pressure fluctuations in large high head propeller turbine." In *IOP Conference Series: Earth and Environmental Science*, vol. 405, no. 1, p. 012032. IOP Publishing, 2019. https://doi.org/10.1088/1755-1315/405/1/012032.

[44] ANSYS. "ANSYS CFX-Solver Theory Guide." *ANSYS Inc* (2023): 724-746.

[45] ANSYS. "ANSYS Fluent-Solver User's Guide." *ANSYS Inc.* (2023).
[46] Yunus Cengel and John Cimbala, *Fluid mechanics: fundamentals and applications*. McGraw-Hill Higher Education. 2006.
[47] S.L. Dixon and C.A. Hall, *Fluid Mechanics and Thermodynamics of Turbomachinery*. Elsevier. 2014: Elsevier.
[48] Gagnon, J. M., and C. Deschênes. "Numerical simulation with flow feature extraction of a propeller turbine unsteady rotor-stator interaction." *Computational Methods and Experimental Measurements XIII* 46 (2007): 55. https://doi.org/10.2495/CMEM070061.
[49] Tran, Bao Ngoc, Haechang Jeong, Jun-Ho Kim, Jin-Soon Park, and Changjo Yang. "Effects of tip clearance size on energy performance and pressure fluctuation of a tidal propeller turbine." *Energies* 13, no. 16 (2020): 4055. https://doi.org/10.3390/en13164055.
[50] Cao, Jingwei, Hong Tian, Soo-Hwang Ahn, Wenzhi Duo, Huili Bi, Lin Zhao, Guozheng Zhao *et al.,* "Fatigue analysis in rotor of a prototype bulb turbine based on fluid-structure interaction." *Engineering Failure Analysis* 132 (2022): 105940. https://doi.org/10.1016/j.engfailanal.2021.105940.
[51] Chen, Huixiang, Daqing Zhou, Yuan Zheng, Shengwen Jiang, An Yu, and You Guo. "Load rejection transient process simulation of a Kaplan turbine model by co-adjusting guide vanes and runner blades." *Energies* 11, no. 12 (2018): 3354. https://doi.org/10.3390/en11123354.
[52] Kan, Kan, Qingying Zhang, Zhe Xu, Huixiang Chen, Yuan Zheng, Daqing Zhou, and Maxima Binama. "Study on a horizontal axial flow pump during runaway process with bidirectional operating conditions." *Scientific Reports* 11, no. 1 (2021): 21834. https://doi.org/10.1038/s41598-021-01250-1.
[53] Trivedi, Chirag, Bhupendra Gandhi, and Cervantes J. Michel. "Effect of transients on Francis turbine runner life: a review." *Journal of Hydraulic Research* 51, no. 2 (2013): 121-132. https://doi.org/10.1080/00221686.2012.732971.
[54] Maulana, Qidun, and Anjar Susatyo. "Numerical simulation of the effect of flow direction angle at inlet boundary condition on flow characteristics and performance of axial flow hydraulic propeller turbine runner." In *2015 International Conference on Sustainable Energy Engineering and Application (ICSEEA)*, pp. 88-94. IEEE, 2015. https://doi.org/10.1109/icseea.2015.7380751.
[55] Qizar, Mohammed Abdullah, Mahmoud L. Mansour, and Shraman Goswami. "Study of steady state and transient blade row CFD methods in a moderately loaded NASA transonic high-speed axial compressor stage." In *Turbo Expo: Power for Land, Sea, and Air*, vol. 55232, p. V06BT37A015. American Society of Mechanical Engineers, 2013. https://doi.org/10.1115/gt2013-94739.
[56] Roache, Patrick J. "Perspective: a method for uniform reporting of grid refinement studies." (1994): 405-413. https://doi.org/10.1115/1.2910291.
[57] Richardson, Lewis Fry. "IX. The approximate arithmetical solution by finite differences of physical problems involving differential equations, with an application to the stresses in a masonry dam." *Philosophical Transactions of the Royal Society of London. Series A, Containing Papers of a Mathematical or Physical Character* 210, no. 459-470 (1911): 307-357. https://doi.org/10.1098/rsta.1911.0009.
[58] LF, RICHARDSON. "The deferred approach to the limit." *Philos. Trans R Soc Lond Ser A* 226 (1927): 223-361. https://doi.org/10.1098/rsta.1927.0008.
[59] Celik, Ishmail B., Urmila Ghia, Patrick J. Roache, and Christopher J. Freitas. "Procedure for estimation and reporting of uncertainty due to discretization in CFD applications." *Journal of fluids Engineering-Transactions of the ASME* 130, no. 7 (2008). https://doi.org/10.1115/1.2960953.
[60] Karaalioglu, Mehmet Salih, and Sakir Bal. "Performance prediction of cavitating marine current turbine by BEMT based on CFD." *Ocean Engineering* 255 (2022): 111221. https://doi.org/10.1016/j.oceaneng.2022.111221.
[61] Celik, Ismail, and Ozgur Karatekin. "Numerical experiments on application of Richardson extrapolation with nonuniform grids." (1997): 584-590. https://doi.org/10.1115/1.2819284.
[62] Liu, Qingsong, Weipao Miao, Qi Ye, and Chun Li. "Performance assessment of an innovative Gurney flap for straight-bladed vertical axis wind turbine." *Renewable Energy* 185 (2022): 1124-1138. https://doi.org/10.1016/j.renene.2021.12.098.
[63] Almohammadi, K. M., D. B. Ingham, L. Ma, and M. Pourkashan. "Computational fluid dynamics (CFD) mesh independency techniques for a straight blade vertical axis wind turbine." *Energy* 58 (2013): 483-493. https://doi.org/10.1016/j.energy.2013.06.012.
[64] (!!! INVALID CITATION !!! [64]).
[65] ANSYS. "ANSYS CFX Reference Guide." *ANSYS INC* (2023): 452.
[66] ANSYS. "ANSYS CFX-Solver Modeling Guide." *ANSYS INC* (2023): 744.
[67] Zhang, Zh. "Master equation, design equations and runaway speed of the Kaplan turbine." *Journal of Hydrodynamics* 33 (2021): 282-300. https://doi.org/10.1007/s42241-021-0020-1.

[68] Date, Abhijit, Aliakbar Akbarzadeh, and Ashwin Date. "Performance investigation of a simple reaction water turbine for power generation from low head micro hydro resources." *Smart Grid and Renewable Energy* 3, no. 03 (2012): 239. https://doi.org/10.4236/sgre.2012.33033.
[69] Shamsoddin, Sina, and Fernando Porté-Agel. "Large eddy simulation of vertical axis wind turbine wakes." *Energies* 7, no. 2 (2014): 890-912. https://doi.org/10.3390/en7020890.
[70] Hunt, Julian CR, Alan A. Wray, and Parviz Moin. "Eddies, streams, and convergence zones in turbulent flows." *Studying turbulence using numerical simulation databases, 2. Proceedings of the 1988 summer program* (1988).
[71] Jeong, Jinhee, and Fazle Hussain. "On the identification of a vortex." *Journal of fluid mechanics* 285 (1995): 69-94. https://doi.org/10.1017/s0022112095000462.
[72] Levy, Yuval, David Degani, and Arnan Seginer. "Graphical visualization of vortical flows by means of helicity." *AIAA journal* 28, no. 8 (1990): 1347-1352. https://doi.org/10.2514/3.25224.
[73] Kumar, Sandeep, Michel J. Cervantes, and Bhupendra K. Gandhi. "Rotating vortex rope formation and mitigation in draft tube of hydro turbines–A review from experimental perspective." *Renewable and Sustainable Energy Reviews* 136 (2021): 110354. https://doi.org/10.1016/j.rser.2020.110354.
[74] Zhang, Yuning, Kaihua Liu, Haizhen Xian, and Xiaoze Du. "A review of methods for vortex identification in hydroturbines." *Renewable and Sustainable Energy Reviews* 81 (2018): 1269-1285. https://doi.org/10.1016/j.rser.2017.05.058.